Velocity-Independent Dry Friction on Mica: Realization of Ideal Amontons-Coulomb Friction

Hiroshi Sakuma,[1,*] Diane E. Moore,[2] David A. Lockner,[2,†] and Toshihiro Kogure[3]

[1]*National Institute for Materials Science, Tsukuba, Japan*
[2]*U.S. Geological Survey, Moffett Field, California 94035, USA*
[3]*University of Tokyo, Hongo, Japan*

(Received 7 January 2026; revised 27 April 2026; accepted 17 June 2026; published 20 July 2026)

The Amontons-Coulomb friction law assumes that the frictional force between materials is independent of sliding velocity. However, as Coulomb noted, this is a rough approximation, and a second-order dependence of friction on the logarithm of sliding velocity is incorporated in a commonly used "rate- and state-dependent" friction representation. Here, we conduct shear experiments on mica, a layer-structured mineral, at temperatures ranging from 22 to 200 °C and under normal stress of 100 MPa. The friction coefficient clearly depends on the logarithmic sliding velocity at 22 °C, but rate sensitivity decreases with increasing temperature until at 200 °C, the friction coefficient is independent of sliding velocity. Our findings could initiate the development of velocity-independent frictional materials, realizing the ideal Amontons-Coulomb friction.

DOI: 10.1103/y3jy-nqcd

According to Amontons-Coulomb friction law, friction between objects is independent of velocity [1–3]. However, in reality, friction between materials weakly depends on the sliding velocity. This velocity-dependent friction is essential for understanding slip stability of materials and earthquakes caused by the movement of natural faults, and has led to the development of what is generally referred to as the "rate- and state-dependent" friction (RSF) formulation in the field of geoscience [4–6]. In the RSF formulation, the friction coefficient μ (= the shear stress divided by the normal stress) of materials is typically described as follows: $\mu = \mu^* + a\ln(V/V^*) + b\ln(V^*\theta/D_c)$. Here, V is sliding velocity, θ is a function of state of the sliding surface, D_c is the characteristic slip distance for strength evolution following a change in sliding velocity, a and b are semi-empirical parameters, and superscript $*$ indicates variable values at reference state. Parameter "a" quantifies the instantaneous response of friction to a change in velocity while "b" quantifies the subsequent evolution of friction with continued slip. The values of these parameters vary with materials and test conditions [7]. While reported values of b typically fall in the range of $-0.02 < b < 0.02$ [7], a is always positive and, to our knowledge, never zero, that is, velocity-independent friction characterized by $a = b = 0$, representing an ideal material described by the velocity-independent Amontons-Coulomb friction law.

The physical and chemical origins of these two parameters are noteworthy. The a parameter is considered to reflect a thermal activation process, characterized by the Arrhenius equation, which occurs at asperity contacts [8–10]. Multiple mechanisms may be involved in this process, such as dislocation glide in layered minerals [11,12], and subcritical crack growth in granite [13]. Within the framework of thermal activation theory, the a value is expected to vary linearly with temperature [8,9], and can be defined as $a = k_B T/\sigma_c \Omega$, where k_B is the Boltzmann constant, T is the temperature, σ_c is the average normal stress at the contacts, and Ω is the activation volume associated with the process [14]. The b parameter is considered to be related to the time-dependent increase in the real area of contact. Its value becomes negligible under dry and vacuum conditions [15,16], indicating that a water-assisted chemical creep process contributes to the increase in the real area of contact over time.

The friction coefficient of layered minerals is much lower than that of materials such as quartz and feldspar [17,18]. Such low friction coefficients have been explained by their nondilatant brittle deformation [19,20] and can be partly explained by low atomic-scale potential barriers between layers for shear [21–25]. These layered materials may also have anomalous friction properties with respect to the sliding velocity. In this Letter, triaxial shear experiments were performed on dry sheets of the layer-structured mineral mica, $KAl_2[Si_3AlO_{10}](OH)_2$, and not using a powdered mica gouge, to measure the velocity dependence of friction at temperatures of 22, 65, 100, and 200 °C and a

*Contact author: sakuma.hiroshi@nims.go.jp
†Contact author: dlockner@usgs.gov

normal stress of 100 MPa. Because of its ability to form atomically flat surfaces via cleavage [26], mica is widely employed in nanotechnology research as a substrate for atomic force microscopy [27] and surface forces apparatus [28,29].

Natural single-crystal mica (muscovite) was used for triaxial shear experiments. The chemical composition of the mica was analyzed by inductively coupled plasma optical emission spectrometry and alizarin complex one-extraction method as $K_{0.92}Na_{0.09}(Al_{1.78}Fe(III)_{0.12}Mg_{0.09}Ti_{0.02})(OH)_{1.96}F_{0.04}[Si_{3.06}Al_{0.94}O_{10}])$. Mica sheets with a thickness of 0.51 mm were rough-cut and then sanded to conform to the elliptical area of driving blocks [Fig. S1(a) [30]]. These sheets were then cleaved to get a clean surface and rinsed with deionized water. The rinsed sheets and novaculite driving blocks were placed in a vacuum oven and dried overnight at 200 °C. The presence of water vapor strongly influences the frictional properties of quartz [15] and clay minerals [56,57]. Such a heating procedure is therefore essential for removing surface water and preventing water adsorption during sample assembly. In our previous study [58], heating at 120 °C for a few hours was found necessary for eliminating adsorbed water on mica, as confirmed by atomic force microscopy.

The sample number and experimental conditions are listed in Table S1 [30]. A standard triaxial test configuration was employed in which a cleaved mica pair was sandwiched between cylindrical driving blocks of porous novaculite (1.905 cm in diameter) with 30° inclined sawcuts [Fig. S1(b) [30]]. The inclined surface of driving blocks was roughened with No. 60 SiC grit to ensure a no-slip interface with the mica samples. After taking novaculite blocks and mica sheets out of the oven, the sample cell was assembled promptly. After the sample assembly was placed in the pressure vessel, it was evacuated with a scroll pump to less than 1% of atmospheric pressure (< -0.099 MPa gauge pressure). A transducer attached to the sample confirmed that this pressure remained constant during each experiment.

Mechanical data were corrected for elastic deformation of the loading system, jacket strength, the confining-pressure dependence of piston seal friction, and the reduction in contact area during deformation [59,60]. Briefly, the confining pressure was applied using argon gas as the confining medium. A soft lead jacket isolated the sample assembly from the argon confining medium. The jacket strength was determined in calibration tests over a range of temperatures and was subtracted from the shear strength measurements. Samples were sheared by advancing a piston against the lower TiC end cap at sliding velocities of 0.01, 0.1, 1.0, and 3.0 μm/s along the shear direction. Axial force was measured using an external load cell. A normal stress of 100 MPa was maintained under computer control by adjusting the confining pressure based on the measured axial force. Axial displacement was measured using an external direct current displacement transducer. Samples were sheared for approximately 3.7 mm of axial displacement. The reduction in contact

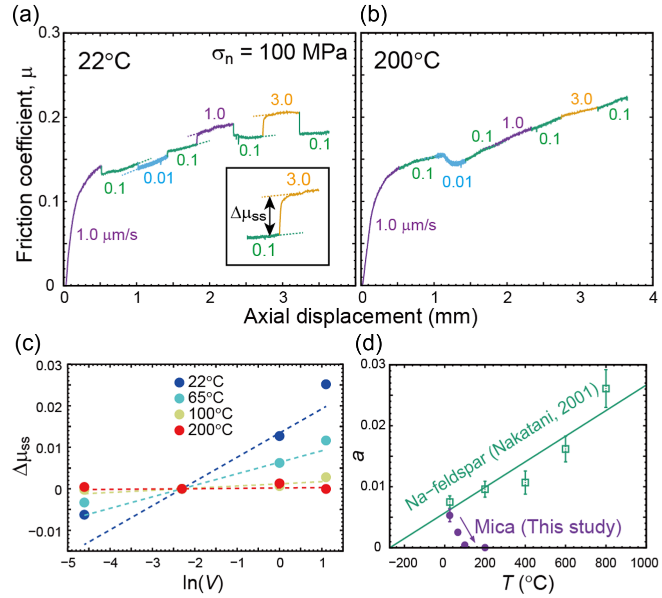

FIG. 1. Friction coefficients of mica and their velocity dependence. Friction coefficients between single crystal micas under the velocity-step tests at 22 °C (a) and 200 °C (b). A difference in the steady-state friction coefficient, $\Delta\mu_{SS}$, is shown in the inset of (a). (c) The change in $\Delta\mu_{SS}$ as a function of sliding velocity and the linear fits (dashed lines), with a reference sliding velocity $V^* = 0.1$ μm/s. (d) The temperature dependence of a values obtained as the slopes of the linear fits to the data in (c).

area at an axial displacement of 3.7 mm was estimated to be 14%, and the normal stress was adjusted accordingly to maintain a constant value of 100 MPa under computer control. The friction force shows a linear relationship with the normal force (Fig. S2).

The surface topographies of the shear planes were observed by secondary electron imaging using a field-emission scanning electron microscope (Hitachi Hi-Tech S-4500) operated at 5 kV. Thin-film specimens for transmission electron microscopy (TEM) analysis were prepared from the surfaces of the shear planes using a focused ion beam system (Hitachi Hi-Tech FB-2100) equipped with a microsampling function. TEM lattice images were acquired using a JEOL JEM-F200 operated at 200 kV in combination with a Gatan OneView high-speed CMOS camera.

Temperature-dependent dry friction of mica—The friction coefficient between (001) mica surfaces is in the range 0.15–0.25 at the tested temperature-pressure conditions [Figs. 1(a), 1(b), S3 [30]], which is consistent with values reported in previous studies [21,58]. The friction coefficient of mica increases generally with mm of accumulated axial displacement but modulates over the microns of the critical slip distance D_c as a function of the imposed sliding velocity ($d\mu_{ss}/d\ln V = a - b = +0.004$) at 22 °C [Fig. 1(c)]. Here, μ_{ss} is the steady-state coefficient of friction at a given velocity. The difference in friction coefficients from the reference sliding velocity of 0.1 μm/s was in the range from -0.01 to $+0.03$ [Fig. 1(c)]. The friction coefficient at 200 °C was comparable to that at 22 °C, but the velocity dependence was no longer observed ($a - b = 0$) [Fig. 1(b)]. The response to the change in the sliding velocity gradually decreased with increasing temperature [Figs. 1(a), 1(b), S3 [30]]. The ~1 MPa stress drop at 1.1 mm axial displacement in the 200 °C experiment [Fig. 1(b)] was an errant instrument adjustment, not the effect of a velocity step. The most likely cause is a realignment of the sample column in response to the lateral shear displacement required for slip on the inclined fault surface.

Which parameter, a or b, controls the variation in the $a - b$ value? Negative b values have been observed in some shear experiments [16], and the variation in the $a - b$ value in our tests may be explained by the combined effects of a positive a and a negative b. However, negative b suggests a decrease in the real area of contact over time, and its physical and chemical origin remains unclear. Commonly, b is known to correlate with the rate of frictional strengthening during stationary hold time in slide-hold-slide tests [7,20,61], allowing b to be measured independent of a. The slide-hold-slide tests (Fig. S4 [30]) confirmed that the strength recovery with time was negligible, that is, $b = 0$. Therefore, the response to the change in sliding velocity is interpreted as being caused by a change in a. The a value calculated by the slope ($d\mu_{ss}/d\ln V$) demonstrates a clear decrease with increasing temperature, reaching zero at 200 °C [Figs. 1(c) and 1(d)]. This phenomenon indicates that mica becomes an ideal Amontons-Coulomb friction material with velocity independence at 200 °C and is a topic for further investigation.

As discussed above, the a value is expected to exhibit a linear relationship with temperature in the framework of thermal activation theory. One representative result [31] showing that a varies linearly with temperature, consistent with the thermal activation theory, was plotted for comparison [Fig. 1(d)]. Although the a values of most minerals remain constant between room temperature and 300 °C and increase at higher temperatures as discussed recently [62] (Fig. S5 [30]), mica shows a negative to neutral temperature dependence of a, up to 200 °C, the highest temperature tested in this Letter. To our knowledge, this behavior has not previously been reported. Nonlinear behavior of the a parameter of materials has been explained by temperature-dependent material properties of σ_c and Ω [14]. For example, the average normal stress at the contacts, σ_c, may decrease with temperature because of the enhancement of plastic deformation at the contact. This may explain the large increase in a at elevated temperatures (> 600 K) of some materials [63]. However, the decrease in a of mica with increasing temperature does not seem to be explained by the changes in σ_c. When the decrease in σ_c occurs at elevated temperatures, the decrease in a requires a large increase in the activation volume, Ω. However, no theory has been established to account for such a large increase in Ω at elevated temperatures.

A mechanism of the realization of Amontons-Coulomb friction—The shear planes of the recovered mica samples exhibit two distinctive characteristics [Fig. 2(a)]. First, slickenlines are present parallel to the shear direction, a common feature in the shear planes of numerous materials. Second, lines perpendicular to the shear direction are evident. The cross section parallel to the shear direction reveals that the lines perpendicular to the shear direction reflect the structure of the ripped off and overlapped surface layers [Fig. 2(b)]. A difference in these surficial structures is not evident among the recovered samples tested from 22 to 200 °C, but a difference in the structure correlated with temperature was observed at 500–1000 nm below the shear surfaces. Some white lines oriented nearly parallel to the shear plane were observed in the recovered sample at 65 °C at 500 nm below the shear plane [Fig. 2(c)]. Most lines correspond to the opening of layers as the bending of layers [Fig. 2(e)], and this would be ripplocations [64,65] (a dislocation of layered materials). Linear features were also observed in the sample tested at 200 °C [Fig. 2(d)], but the depth extent from 100 to 300 nm seems to be shallower than those at lower temperature and bending of the layer was not observed at 200 °C [Fig. 2(f)]. The white linear lines at 200 °C are considered to indicate that the region has become amorphous due to electron beam damage during the initial stage of TEM observation.

Based on observations of the recovered samples, we postulate that mica's instantaneous response to a change in velocity, characterized by the RSF a parameter, reflects the shear response of ripplocations. Nonequilibrium molecular dynamics (NEMD) simulations were conducted to evaluate the a value for mica models without dislocations [Fig. 3(a)] and those containing ripplocations [Fig. 3(b)]. Force field of mica used in this Letter is an interatomic potential model, and it has been developed to reproduce the mica structure and physical properties [32–34]. The normal stress of 6 GPa was chosen because the normal stress of real area of contact can be approximated by the indentation hardness [21,66], by assuming the contacts are yielding normal to the interface. Shear strain was applied along the $\langle 100 \rangle$ sliding direction on the (001) plane. The a value was calculated based on the differences in steady-state friction coefficients at different tested sliding velocities. The sliding velocities at the top layer of the supercell relative to the bottom layer can be on the order of 1 m/s at a shear rate of 10^9 s^{-1} and 100 m/s at 10^{11} s^{-1}. These velocities are much higher than those used in experimental sliding tests due to the computational cost (see simulation details in Supplemental Material [30]). The structures of mica were drawn using VESTA [67].

At lower shear rates (10^9 and 10^{10} s^{-1}), the sliding velocity remains much higher than in shear experiments; however, the shear stress-strain behavior of dislocation-free mica [Fig. 3(c)] resembles that obtained from density-functional-theory calculations at nominally zero velocity [21], suggesting that the friction mechanism is similar to

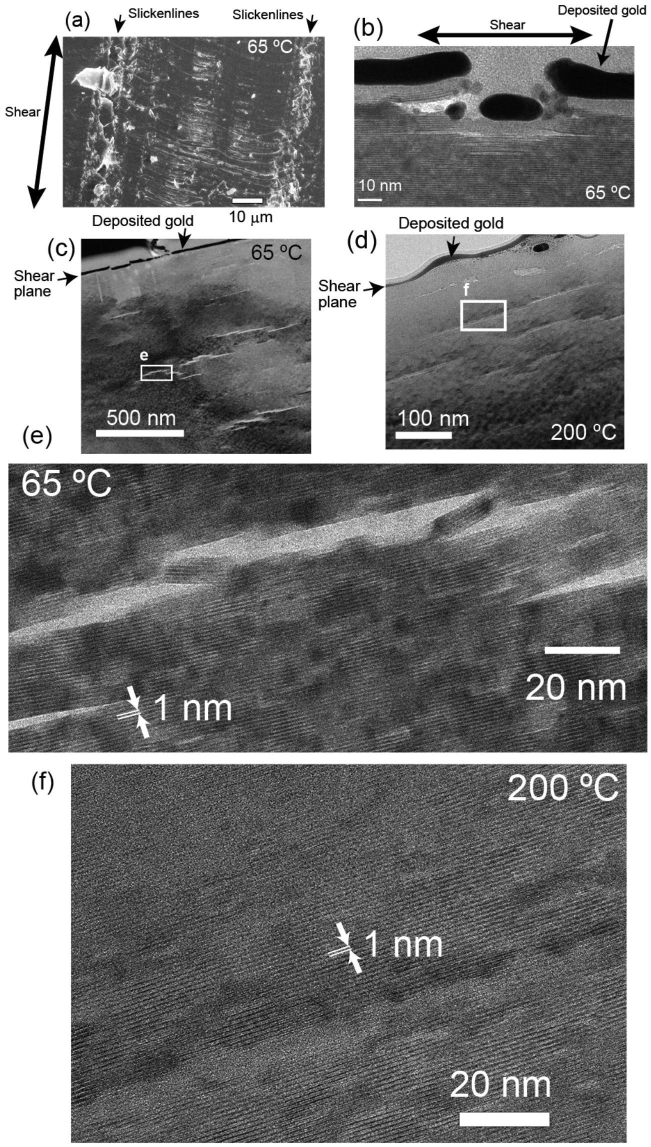

FIG. 2. Structures of the sheared surface and cross sections. (a) Scanning electron microscope (SEM) image of the recovered shear plane tested at 65 °C, (b) transmission electron microscopy (TEM) image of the cross section near the surface, and TEM images of the cross section from surface to depth tested at 65 °C [(c),(e)] and 200 °C [(d),(f)]. White lines are observed in both cross sections at low magnification [(c),(d)], whereas high-magnification images reveal that the white lines observed at 65 °C correspond to bending of the layers [(e)], and those observed at 200 °C may correspond to amorphous regions caused by electron-beam damage [(f)]. The shear direction is indicated by arrows [(a),(b)]. The black material on the surface is the gold deposited for the SEM observation. The thickness of 1 nm corresponds to the thickness of single mica layer.

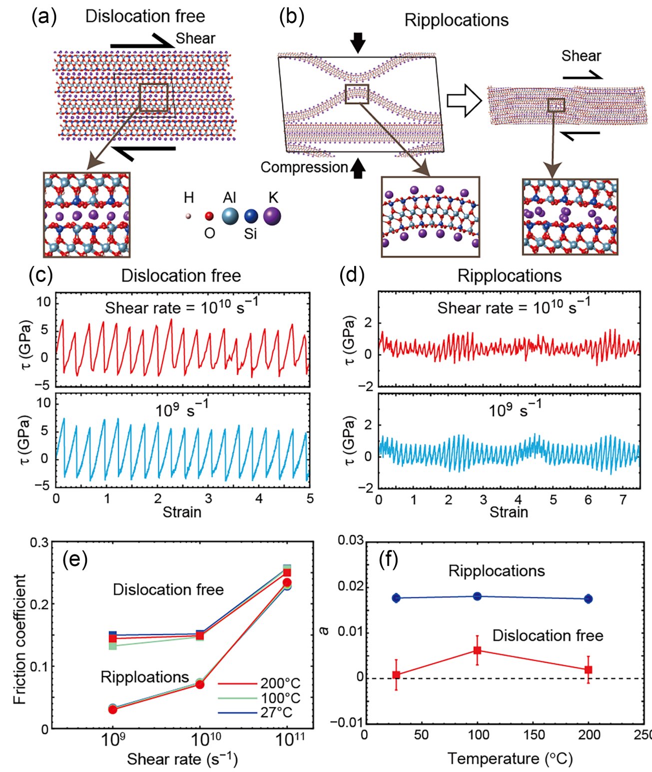

FIG. 3. Friction coefficients of dislocation-free and ripplocation-bearing mica obtained by NEMD simulations. (a) Dislocation-free mica model and (b) ripplocation-bearing mica model for NEMD simulations, (c) shear stress versus strain of the dislocation-free model at 200 °C, (d) shear stress versus strain of the ripplocation-bearing model at 200 °C, (e) calculated friction coefficients, and (f) a values in the RSF formulation. High normal and shear stresses on the order of GPa are required to simulate the real area of contact. The experimental shear stress at a normal stress of 100 MPa can be estimated by multiplying the ratio of real area of contact to the apparent contact area.

that at nominally zero velocity. Moreover, the friction coefficient of 0.15, which is comparable to experimental observations [21], supports the notion that the effect of sliding velocity is negligible for simulations at shear rates $\leq 10^{10}$ s^{-1}. The friction coefficient of the dislocation-free model at shear rates of 10^9 and 10^{10} s^{-1} appears to be independent of sliding velocity [Fig. 3(e)], and the calculated a values are nearly zero for the dislocation-free model [Fig. 3(f)]. The increased friction coefficients at 10^{11} s^{-1} can be attributed to a change in the friction mechanism. At such extremely high sliding velocities, interlayer ions cannot reach the potential energy minimum configuration because the sliding velocity exceeds the velocity of phonon vibrations. The interionic potential force acting on the ions becomes the source of friction. Therefore, the results at 10^{11} s^{-1} cannot be compared with our experiments.

In contrast, the ripplocation-bearing model exhibited low shear stress [Fig. 3(d)] and strong velocity dependence at these sliding velocities of 10^9 and 10^{10} s^{-1} [Fig. 3(e)]. The calculated a values for ripplocations, derived from velocity changes between 10^9 and 10^{10} s^{-1}, were positive and constant across the temperature range of 27 to 200 °C [Fig. 3(f)]. The presence of ripplocations in low-temperature samples and their absence in high-temperature samples, as confirmed by cross-sectional observations of sheared specimens, suggests that the absence of ripplocations is associated with the velocity-independent frictional behavior of mica at 200 °C.

Our findings indicate that the physics underlying the a values of mica are connected to the presence of ripplocations. TEM observations did not detect ripplocations in fresh mica, suggesting that applied shear and normal stress caused the layers to buckle and form ripplocations. The formation and stability of ripplocations are influenced by three main components: the elastic energy associated with out-of-plane deformation, the adhesion energy related to interlayer separation, and interlayer friction that facilitates layer sliding [68]. Thermal effects can alter these components in both directions. Under our tested conditions, thermal expansion of mica may increase the elastic energy associated with out-of-plane deformation, resulting in the decrease of ripplocations at elevated temperatures.

The velocity-independent friction confirmed in mica at $T = 200\,°\mathrm{C}$ is a realization of ideal Coulomb's velocity-independent friction. If ideal Amontons-Coulomb friction material is realized at various temperature conditions, such material can be useful as a lubricant among mechanical parts because it requires no precise control of friction depending on the sliding velocity. The case where $a = b = 0$ removes all rate dependence in the RSF model, making the use of this formalism unnecessary. This velocity-independent friction of mica must be realized due to the layered structure. In our analysis, velocity dependence of dislocations (ripplocations) in the layered materials is the origin of the a value in the RSF model. The elimination of ripplocations in layered materials may be a crucial step toward realizing an ideal friction material, exhibiting velocity-independent behavior.

Acknowledgments—We thank Brian D. Kilgore, Nicholas M. Beeler, and two anonymous reviewers for useful comments. The NEMD calculations were conducted using the Numerical Materials Simulator at NIMS. We thank A. Iwanade for his assistance with inductively coupled plasma optical emission spectrometry analysis. Any use of trade, firm, or product names is for descriptive purposes only and does not imply endorsement by the U.S. Government. This work was supported by JSPS KAKENHI Grants No. JP24K00795, No. JP25H00688, and No. JP20K04115.

Data availability—The data that support the findings of this article are openly available [69,70].

[1] M. Amontons, De la resistance cause'e dans les machines, Hist. l'Acad. R. Sci. 206 (1699).

[2] C. A. Coulomb, *Théorie Des Machines Simples En Ayant Égard Au Frottement de Leurs Parties et à La Roideur Des Cordages* (Bachelier Imprimeur, Paris, 1821).

[3] Y. Desplanques, Amontons-Coulomb friction laws, A review of the original manuscript, SAE Int. J. Mater. Manuf. **8**, 98 (2015).

[4] J. H. Dieterich, Modeling of rock friction: 1. Experimental results and constituve equations, J. Geophys. Res. **84**, 2161 (1979).

[5] A. Ruina, Slip instability and state variable friction laws, J. Geophys. Res. **88**, 10359 (1983).

[6] C. Marone, Laboratory-derived friction laws and their application to seismic faulting, Annu. Rev. Earth Planet Sci. **26**, 643 (1998).

[7] M. J. Ikari, B. M. Carpenter, and C. Marone, A microphysical interpretation of rate- and state-dependent friction for fault gouge, Geochem. Geophys. Geosyst. **17**, 1660 (2016).

[8] F. Heslot, T. Baumberger, B. Perrin, B. Caroli, and C. Caroli, Creep, stick-slip, and dry-friction dynamics: Experiments and a heuristic model, Phys. Rev. E **49**, 4973 (1994).

[9] N. H. Sleep, Application of a unified rate and state friction theory to the mechanics of fault zones with strain localization, J. Geophys. Res. **102**, 2875 (1997).

[10] R. M. Stesky, Mechanisms of high temperature frictional sliding in westerly granite, Can. J. Earth. Sci. **15**, 361 (1978).

[11] N. M. Beeler, T. E. Tullis, A. K. Kronenberg, and L. A. Reinen, The instantaneous rate dependence in low temperature laboratory rock friction and rock deformation experiments, J. Geophys. Res. **112**, 1 (2007).

[12] L. A. Reinen, T. E. Tullis, and J. D. Weeks, Two-mechanism model for frictional sliding of serpentinite, Geophys. Res. Lett. **19**, 1535 (1992).

[13] D. A. Lockner, A generalized law for brittle deformation of Westerly granite, J. Geophys. Res. **103**, 5107 (1998).

[14] J. R. Rice, N. Lapusta, and K. Ranjith, Rate and state dependent friction and the stability of sliding between elastically deformable solids, J. Mech. Phys. Solids **49**, 1865 (2001).

[15] J. H. Dieterich and G. Conrad, Effect of humidity on time-dependent and velocity-dependent friction in rocks, J. Geophys. Res. **89**, 4196 (1984).

[16] M. L. Blanpied, C. J. Marone, D. A. Lockner, J. D. Byerlee, and D. P. King, Quantitative measure of the variation in fault rheology due to fluid-rock interactions, J. Geophys. Res. **103**, 9691 (1998).

[17] J. Byerlee, Friction of Rocks, Pure Appl. Geophys. **116**, 615 (1978).

[18] D. E. Moore and D. A. Lockner, Crystallographic controls on the frictional behavior of dry and water-saturated sheet structure minerals, J. Geophys. Res. **109**, B03401 (2004).

[19] J. Escartín, G. Hirth, and B. Evans, Nondilatant brittle deformation of serpentinites: Implications for Mohr-Coulomb theory and the strength of faults, J. Geophys. Res. **102**, 2897 (1997).

[20] N. M. Beeler, 13. Laboratory-observed faulting in intrinsically, and apparently weak materials: Strength, seismic coupling, dilatancy, and pore-fluid pressure, in *The Seismogenic Zone of Subduction Thrust Faults*, edited by T. H. Dixon and C. Moore (Columbia University Press, New York Chichester, West Sussex, 2007), pp. 370–449.

[21] H. Sakuma, K. Kawai, I. Katayama, and S. Suehara, What is the origin of macroscopic friction?, Sci. Adv. **4**, eaav2268 (2018).

[22] H. Sakuma, K. Kawai, and T. Kogure, Interlayer energy of pyrophyllite: Implications for macroscopic friction, Am. Mineral. **105**, 1204 (2020).

[23] H. Sakuma, D. A. Lockner, J. Solum, and N. C. Davatzes, Friction in clay-bearing faults increases with the ionic radius of interlayer cations, Commun. Earth Environ. **3**, 116 (2022).

[24] H. Okuda, K. Kawai, and H. Sakuma, First-principles investigation of frictional characteristics of brucite: An application to its macroscopic frictional characteristics, J. Geophys. Res. Solid Earth **124**, 10423 (2019).

[25] H. Okuda, K. Kawai, and H. Sakuma, Atomic-scale interlayer friction of gibbsite is lower than brucite due to interactions of hydroxyls, Am. Mineral. **108**, 1476 (2023).

[26] W. De Poel, S. Pintea, J. Drnec, F. Carla, R. Felici, P. Mulder, J. A. A. W. Elemans, W. J. P. Van Enckevort, A. E. Rowan, and E. Vlieg, Muscovite mica: Flatter than a pancake, Surf. Sci. **619**, 19 (2014).

[27] Y. L. Lyubchenko, L. S. Shlyakhtenko, and T. Ando, Imaging of nucleic acids with atomic force microscopy, Methods **54**, 274 (2011).

[28] J. N. Israelachvili, *Intermolecular and Surface Forces.* 3rd ed. (Academic Press, San Diego, 2011).

[29] H. Sakuma, K. Otsuki, and K. Kurihara, Viscosity and lubricity of aqueous NaCl solution confined between mica surfaces studied by shear resonance measurement, Phys. Rev. Lett. **96**, 046104 (2006).

[30] See Supplemental Material at http://link.aps.org/supplemental/10.1103/y3jy-nqcd for supplemental notes about experimental details, supplemental figures about the friction coefficients at 65 and 100 °C, relationship between shear stress and normal stress, the results of slide-hold-slide test at 22 and 200 °C, available temperature dependence of the *a* parameter of various materials, and computational details, which includes Refs. [16,21,31–55].

[31] M. Nakatani, Conceptual and physical clarification of rate and state friction: Frictional sliding as a thermally activated rheology, J. Geophys. Res. **106**, 13347 (2001).

[32] H. Sakuma, T. Kondo, H. Nakao, K. Shiraki, and K. Kawamura, Structure of hydrated sodium ions and water molecules adsorbed on the mica/water interface, J. Phys. Chem. C **115**, 15959 (2011).

[33] H. Sakuma and K. Kawamura, Structure and dynamics of water on Li^+-, Na^+-, K^+-, Cs^+-, H_3O^+-exchanged muscovite surfaces: A molecular dynamics study, Geochim. Cosmochim. Acta **75**, 63 (2011).

[34] H. Sakuma and K. Kawamura, Structure and dynamics of water on muscovite mica surfaces, Geochim. Cosmochim. Acta **73**, 4100 (2009).

[35] A. M. H. Pluymakers and A. R. Niemeijer, Healing and sliding stability of simulated anhydrite fault gouge: Effects of water, temperature and CO_2, Tectonophysics **656**, 111 (2015).

[36] C. He, W. Tan, and L. Zhang, Comparing dry and wet friction of plagioclase: Implication to the mechanism of frictional evolution effect at hydrothermal conditions, J. Geophys. Res. Solid Earth **121**, 6365 (2016).

[37] C. He, L. Luo, Q. M. Hao, and Y. Zhou, Velocity-weakening behavior of plagioclase and pyroxene gouges and stabilizing effect of small amounts of quartz under hydrothermal conditions, J. Geophys. Res. Solid Earth **118**, 3408 (2013).

[38] M. Takahashi, S. I. Uehara, K. Mizoguchi, I. Shimizu, K. Okazaki, and K. Masuda, On the transient response of serpentine (antigorite) gouge to stepwise changes in slip velocity under high-temperature conditions, J. Geophys. Res. **116**, B10405 (2011).

[39] P. Tian and C. He, Velocity weakening of simulated augite gouge at hydrothermal conditions: Implications for frictional slip of pyroxene-bearing mafic lower crust, J. Geophys. Res. Solid Earth **124**, 6428 (2019).

[40] Z. Lu and C. He, Frictional behavior of simulated biotite fault gouge under hydrothermal conditions, Tectonophysics **622**, 62 (2014).

[41] Z. Lu and C. He, Friction of foliated fault gouge with a biotite interlayer at hydrothermal conditions, Tectonophysics **740–741**, 72 (2018).

[42] Y. Liu and C. He, Friction properties of hornblende and implications for slow-slip events in subduction zones, Tectonophysics **796**, 228644 (2020).

[43] E. K. Mitchell, Y. Fialko, and K. M. Brown, Velocity-weakening behavior of Westerly granite at temperature up to 600 °C, J. Geophys. Res. Solid Earth **121**, 6932 (2016).

[44] S. A. M. den Hartog, A. R. Niemeijer, and C. J. Spiers, New constraints on megathrust slip stability under subduction zone P-T conditions, Earth Planet. Sci. Lett. **353–354**, 240 (2012).

[45] A. R. Niemeijer and R. L. M. Vissers, Earthquake rupture propagation inferred from the spatial distribution of fault rock frictional properties, Earth Planet. Sci. Lett. **396**, 154 (2014).

[46] C. Boulton, D. E. Moore, D. A. Lockner, V. G. Toy, J. Townend, and R. Sutherland, Frictional properties of exhumed fault gouges in DFDP-1 cores, Alpine Fault, New Zealand, Geophys. Res. Lett. **41**, 356 (2014).

[47] R. D. Valdez, H. Kitajima, and D. M. Saffer, Effects of temperature on the frictional behavior of material from the Alpine Fault Zone, New Zealand, Tectonophysics **762**, 17 (2019).

[48] M. Sawai, A. R. Niemeijer, O. Plümper, T. Hirose, and C. J. Spiers, Nucleation of frictional instability caused by fluid pressurization in subducted blueschist, Geophys. Res. Lett. **43**, 2543 (2016).

[49] N. Hellebrekers, A. R. Niemeijer, Å. Fagereng, B. Manda, and R. L. S. Mvula, Lower crustal earthquakes in the East African Rift System: Insights from frictional properties of rock samples from the Malawi rift, Tectonophysics **767**, 228167 (2019).

[50] H. S. Rabinowitz, H. M. Savage, R. M. Skarbek, M. J. Ikari, B. M. Carpenter, and C. Collettini, Frictional behavior of input sediments to the Hikurangi Trench, New Zealand, Geochem. Geophys. Geosyst. **19**, 2973 (2018).

[51] S. A. M. den Hartog, M. Y. Thomas, and D. R. Faulkner, How do laboratory friction parameters compare with observed fault slip and geodetically derived friction parameters? Insights from the longitudinal valley fault, Taiwan, J. Geophys. Res. Solid Earth **126**, e2021JB022390 (2021).

[52] L. Zhang and C. He, Frictional properties of phyllosilicate-rich mylonite and conditions for the brittle-ductile transition, J. Geophys. Res. Solid Earth **121**, 3017 (2016).

[53] S. A. M. den Hartog, C. Marone, and D. M. Saffer, Frictional behavior downdip along the subduction megathrust: Insights from laboratory experiments on exhumed samples at *in situ* conditions, J. Geophys. Res. Solid Earth **128**, e2022JB024435 (2023).

[54] M. Sawai, A. R. Niemeijer, T. Hirose, and C. J. Spiers, Frictional properties of JFAST core samples and implications for slow earthquakes at the Tohoku subduction zone, Geophys. Res. Lett. **44**, 8822 (2017).

[55] P. P. Ewald, Die Berechnung optischer und elektrostatischer Gitterpotentiale, Ann. Phys. (N.Y.) **369**, 253 (1921).

[56] M. J. Ikari, D. M. Saffer, and C. Marone, Effect of hydration state on the frictional properties of montmorillonite-based fault gouge, J. Geophys. Res. **112**, B06423 (2007).

[57] H. Tetsuka, I. Katayama, H. Sakuma, and K. Tamura, Effects of humidity and interlayer cations on the frictional strength of montmorillonite, Earth Planets Space **70**, 56 (2018).

[58] K. Kawai, H. Sakuma, I. Katayama, and K. Tamura, Frictional characteristics of single and polycrystalline muscovite and influence of fluid chemistry, J. Geophys. Res. Solid Earth **120**, 6209 (2015).

[59] D. E. Moore and D. A. Lockner, Frictional strengths of talc-serpentine and talc-quartz mixtures, J. Geophys. Res. **116**, B01403 (2011).

[60] S. Tembe, D. A. Lockner, and T.-F. Wong, Effect of clay content and mineralogy on frictional sliding behavior of simulated gouges: Binary and ternary mixtures of quartz, illite, and montmorillonite, J. Geophys. Res. **115**, B03416 (2010).

[61] T. Tesei, C. Collettini, B. M. Carpenter, C. Viti, and C. Marone, Frictional strength and healing behavior of phyllosilicate-rich faults, J. Geophys. Res. **117**, B09402 (2012).

[62] S. Barbot, Does the direct effect of friction increase continuously with absolute temperature?, Proc. Natl. Acad. Sci. U.S.A. **121**, e2405111121 (2024).

[63] H. Noda, Frictional constitutive law at intermediate slip rates accounting for flash heating and thermally activated slip process, J. Geophys. Res. **113**, B09302 (2008).

[64] A. Kushima, X. Qian, P. Zhao, S. Zhang, and J. Li, Ripplocations in van der Waals layers, Nano Lett. **15**, 1302 (2015).

[65] J. Aslin, E. Mariani, K. Dawson, and M. W. Barsoum, Ripplocations provide a new mechanism for the deformation of phyllosilicates in the lithosphere, Nat. Commun. **10**, 686 (2019).

[66] J. H. Dieterich and B. D. Kilgore, Imaging surface contacts: Power law contact distributions and contact stresses in quartz, calcite, glass and acrylic plastic, Tectonophysics **256**, 219 (1996).

[67] K. Momma and F. Izumi, VESTA 3 for three-dimensional visualization of crystal, volumetric and morphology data, J. Appl. Crystallogr. **44**, 1272 (2011).

[68] J. G. McHugh, P. Mouratidis, and K. Jolley, Ripplocations in layered materials: Sublinear scaling and basal climb, Phys. Rev. B **103**, 195436 (2021).

[69] D. A. Lockner, H. Sakuma, and D. E. Moore, *Data Release for Velocity-Independent Dry Friction on Mica Experiments*, edited by D. A. Lockner, H. Sakuma, and D. E. Moore, U.S. Geological Survey Data Release (2026), 10.5066/P14QKMWB.

[70] H. Sakuma, A dataset of molecular dynamics simulations of velocity-independent dry friction on mica, Mendeley Data, V1, (2026), 10.17632/442368m5fb.1.